

# Accelerating High-Order Mesh Optimization Using Finite Element Partial Assembly on GPUs

Jean-Sylvain Camier<sup>1</sup>, Veselin Dobrev<sup>1</sup>, Patrick Knupp<sup>2</sup>, Tzanio Kolev<sup>1</sup>, Ketan Mittal<sup>1</sup>,  
Robert Rieben<sup>1</sup>, Vladimir Tomov<sup>1</sup>

---

## Abstract

In this paper we present a new GPU-oriented mesh optimization method based on high-order finite elements. Our approach relies on node movement with fixed topology, through the Target-Matrix Optimization Paradigm (TMOP) and uses a global nonlinear solve over the whole computational mesh, i.e., all mesh nodes are moved together. A key property of the method is that the mesh optimization process is recast in terms of finite element operations, which allows us to utilize recent advances in the field of GPU-accelerated high-order finite element algorithms. For example, we reduce data motion by using tensor factorization and matrix-free methods, which have superior performance characteristics compared to traditional full finite element matrix assembly and offer advantages for GPU-based HPC hardware. We describe the major mathematical components of the method along with their efficient GPU-oriented implementation. In addition, we propose an easily reproducible mesh optimization test that can serve as a performance benchmark for the mesh optimization community.

*Keywords:* mesh optimization, GPUs, performance benchmark, finite elements, curved meshes, HPC, high-order, matrix-free methods, TMOP

---

## 1. Introduction

The rise of heterogeneous architectures, such as general-purpose GPUs, has motivated a rethinking of the algorithms used in large-scale, high-performance simulations [1]. The

---

\*Performed under the auspices of the U.S. Department of Energy under Contract DE-AC52-07NA27344 (LLNL-JRNL-835500)

<sup>1</sup>Lawrence Livermore National Laboratory, 7000 East Avenue, Livermore, CA 94550

<sup>2</sup>Dihedral LLC, Bozeman, MT 59715

new computing systems favor algorithms that expose ultra fine-grain parallelism and maximize the ratio of floating point operations to energy-intensive data movement. As more applications are porting their codes to GPU systems, meshing algorithms can become a bottleneck unless they can be formulated in a balanced, data-parallel way. Some of the existing mesh optimization methods are not a good match for the new architectures because they rely on geometric operations and local topology changes that introduce branching and load imbalance between parallel threads.

In this paper we present a computationally efficient GPU-capable mesh optimization method based on high-order finite elements (FE). Starting with our existing mesh optimization FE framework [2], we reformulate all FE kernels using the so-called partial assembly (PA) technique, and implement the resulting formulation through a general abstraction that allows both CPU and GPU execution. Partial assembly is a technique introduced in the pioneering work of Deville, Fischer, and Mund [3], where the authors demonstrate that by using a tensor product of 1D basis functions, fully assembled operators do not need to be stored anymore and the computational cost associated with the storage, assembly, and evaluation of partially assembled operators reduces to  $\mathcal{O}(p^d)$ ,  $\mathcal{O}(p^d)$ , and  $\mathcal{O}(p^{d+1})$  per element, respectively, where  $p$  is the polynomial order of the FE space and  $d$  is the space dimension. The traditional FE approach of pre-assembling and storing sparse matrices, on the other hand, leads to much worse computational costs per element, namely,  $\mathcal{O}(p^{2d})$  for storage,  $\mathcal{O}(p^{3d})$  for assembly, and  $\mathcal{O}(p^{2d})$  for evaluation. Obtaining the above PA complexities, however, requires that the finite element basis functions are tensor products of 1D basis functions, e.g., quadrilaterals in 2D and hexahedra in 3D. Partial assembly has become even more relevant in recent years [4, 5, 6] owing to its efficient use of GPU-based architectures, which are desirable for arithmetically intensive applications that do not require a large amount of data to be moved between the CPU and GPU [1].

The presented algorithms are developed in the context of the Target-Matrix Optimization Paradigm (TMOP) for high-order meshes [2, 7] and its implementation in the MFEM finite element library [8]. TMOP minimizes a functional that depends on each element’s current and target (desired) geometric parameters: element *aspect-ratio*, *size*, *skew*, and *orientation*, which allows us to optimize and adapt the mesh to improve the accuracy and computational

cost of FEM calculations (see, e.g., Section 4.1 of [9]). The TMOP-based methodology is purely algebraic, extends to both simplices and hexahedra/quadrilaterals of any order, and supports nonconforming isotropic and anisotropic refinements in 2D and 3D. Similar methods in the literature include Laplacian smoothing, where each node is typically moved as a linear function of the positions of its neighbors [10, 11, 12], optimization-based smoothing, where a functional based on elements’ geometrical parameters is minimized [13, 14, 15, 16, 17, 18], and equidistribution with respect to an appropriate metric tensor [19, 20, 21], amongst others [22, 23, 24].

A survey of the literature shows that despite the introduction of recent mesh optimization strategies on GPU-based architectures, the notion of partial assembly is not present in the field of mesh optimization. This is likely because most existing methods are either developed for low-order meshes [25, 26] or use a localized approach (such as Laplacian smoothing or optimization-based smoothing with a sequential patch-by-patch approach) [27, 26, 28, 29]. In contrast to other approaches, the variational-based TMOP methods are well-suited to GPU acceleration, as all of the operations can be recast in the form of finite element computations, allowing us to take advantage of the significant GPU advances in this area. In particular, matrix-free algorithms and partial assembly of nonlinear forms, such as the global TMOP functional, can lead to orders-of-magnitude reduction in the runtime of high-order applications compared to traditional matrix-based algorithms [30].

The remainder of the paper is organized as follows. Section 2 gives an overview of preliminaries such as high-order mesh representation and the TMOP-based mesh adaptation framework, that are essential for understanding our method. In Section 3, we describe the fundamentals of partial assembly for high-order FEM operators. Here, we also describe our methodology for partial assembly of TMOP-based mesh optimization methods. In Section 4, we present several numerical examples and benchmarks demonstrating the improvement in computational efficiency due to use of partial assembly on GPU-based architectures in comparison to full-assembly on CPUs. Finally, we close with directions for future work in Section 5.

## 2. Preliminaries

This section provides a basic description of the TMOP-based  $r$ -adaptivity algorithm that is the starting point of our work. We only focus on the aspects that are relevant to the description of partial assembly of TMOP on GPUs. See [2, 7] for additional details.

### 2.1. Discrete Mesh Representation

In our finite element based framework, the domain  $\Omega \subset \mathbb{R}^d$  is discretized as a union of curved mesh elements of order  $p$ . To obtain a discrete representation of these elements, we select a set of scalar basis functions  $\{\bar{w}_i\}_{i=1}^{N_p}$ , on the reference element  $\bar{E}$ . In the case of tensor-product elements (quadrilaterals in 2D, hexahedra in 3D) which is the focus of this paper,  $N_p = (p+1)^d$ , and the basis spans the space of all polynomials of degree at most  $p$  in each variable, denoted by  $Q_p$ . The position of an element  $E$  in the mesh  $\mathcal{M}$  is fully described by a matrix  $\mathbf{x}_E$  of size  $d \times N_p$  whose columns represent the coordinates of the element *control points* (also known as *nodes* or element *degrees of freedom*). Given  $\mathbf{x}_E$ , we introduce the map  $\Phi_E : \bar{E} \rightarrow \mathbb{R}^d$  whose image defines the physical element  $E$ :

$$x(\bar{x}) = \Phi_E(\bar{x}) \equiv \sum_{i=1}^{N_p} \mathbf{x}_{E,i} \bar{w}_i(\bar{x}), \quad \bar{x} \in \bar{E}, \quad x = x(\bar{x}) \in E, \quad (1)$$

where  $\mathbf{x}_{E,i}$  denotes the  $i$ -th column of  $\mathbf{x}_E$ , i.e., the  $i$ -th node of element  $E$ . To represent the whole mesh, the coordinates of the control points of every element are arranged in a global vector  $\mathbf{x}$  of size  $d \times N_x$  that stores the coordinates of all node positions and ensures continuity at the faces of all elements. Here  $N_x$  is the global number of control points for a principal direction.

### 2.2. TMOP for $r$ -adaptivity

In this subsection we summarize the main components of the TMOP approach; all details of the specific method we use are provided in [7]. The input of TMOP is the user-specified transformation matrix  $W$ , from reference-space  $\bar{E}$  to target element  $E_t$ , which represents the ideal geometric properties desired for every mesh point. Note that after discretization, there will be multiple input transformation matrices  $W$  – one for every quadrature point in

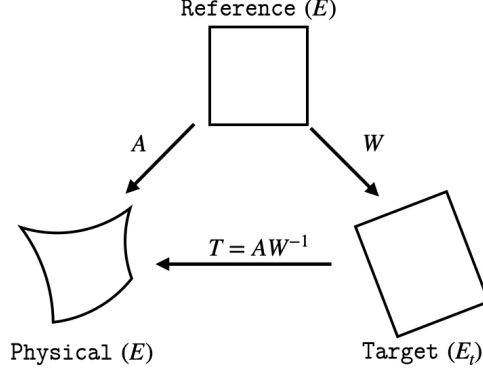


Figure 1: Schematic representation of the major TMOP matrices.

every mesh element. The construction of this transformation is guided by the fact that any Jacobian matrix can be written as a composition of four components:

$$W = \underbrace{\zeta}_{[\text{volume}]} \underbrace{R}_{[\text{rotation}]} \underbrace{Q}_{[\text{skewness}]} \underbrace{D}_{[\text{aspect ratio}]} . \quad (2)$$

Further details and a thorough discussion on how TMOP’s target construction methods encode geometric information into the target matrix  $W$  is given by Knupp in [31]. In the context of  $r$ -adaptivity the geometric parameters of (2) are typically constructed using a discrete PDE solution available on the initial mesh. As the nodal coordinates change during the optimization process, these discrete functions are mapped to the updated mesh so that  $W$  can be constructed at each reference point, see Section 4 in [32].

Using (1), the Jacobian  $A$  of the mapping  $\Phi_E$  from the reference coordinates  $\bar{x} \in \bar{E}$  to the current physical-space coordinates  $x \in E$  is defined as

$$A(\bar{x}) = \frac{\partial \Phi_E}{\partial \bar{x}} = \sum_{i=1}^{N_p} \mathbf{x}_{E,i} [\nabla \bar{w}_i(\bar{x})]^T, \quad \bar{x} \in \bar{E}. \quad (3)$$

Combining (3) and (2), the transformation from the target coordinates to the current physical coordinates, see Figure 1, is defined as

$$T = AW^{-1}. \quad (4)$$

The matrix  $T$  is then used to define a quality metric  $\mu(T)$  that measures the difference between  $A$  and  $W$  in terms of the geometric parameters of interest specified in (2). For example,  $\mu_2 = |T|^2/2\tau - 1$  is a *shape* metric that depends on the skew and aspect ratio

components, but is invariant to orientation and volume. Here,  $|T|$  is the Frobenius norm of  $T$  and  $\tau = \det(T)$ . Similarly,  $\mu_{55} = (\tau - 1)^2$  is a *size* metric that depends only on the volume of the element. There are also *shape+size* metrics such as  $\mu_7 = |T - T^{-t}|^2$  or  $\mu_9 = \tau|T - T^{-t}|^2$  that depend on volume, skew and aspect ratio, but are invariant to orientation. A list of metrics along with their theoretical properties can be found in [33].

The quality metric  $\mu(T)$  is used to define the TMOP objective function: for any given vector  $\mathbf{x}$  of node positions, we define

$$F(\mathbf{x}) = \sum_{E \in \mathcal{M}} \int_{E_t} \omega(x_t) \mu(T(x_t)) dx_t + \sum_{E \in \mathcal{M}} \int_{E_t} \xi(x - x_0, \delta(x_0)) dx_t, \quad (5)$$

where  $x = x(\bar{x}) = x(\bar{x}(x_t))$  is the element  $E$  mapping defined by  $\mathbf{x}$ ,  $E_t$  is the target element corresponding to the physical element  $E$ ,  $\omega$  is a user-prescribed spatial weight, and the integral involving  $\xi(x - x_0, \delta(x_0))$  limits the node displacements in a user-specified manner (a typical choice is  $\xi(y, \delta) = |y|^2/\delta^2$ ) with  $x_0 = x_0(\bar{x}) = x_0(\bar{x}(x_t))$  being a given initial/reference mesh position. The integrals are computed with a standard quadrature rule. The mesh is optimized by minimizing the objective  $F$  through node movement. More specifically, we solve  $\partial F(\mathbf{x})/\partial \mathbf{x} = 0$  with a nonlinear solver, e.g., Newton's method. The gradient  $\partial F$  and Hessian  $\partial^2 F$  of  $F$  are discussed in further detail in Sections 3.3 and 3.4.

Figure 2 shows an example of  $r$ -adaptivity to a discrete material indicator using TMOP to control the aspect-ratio and the size of the elements in a mesh. In this example, the material indicator function is used to define discrete functions for aspect-ratio and size targets in (2), and the mesh is optimized using a *shape+size* metric.

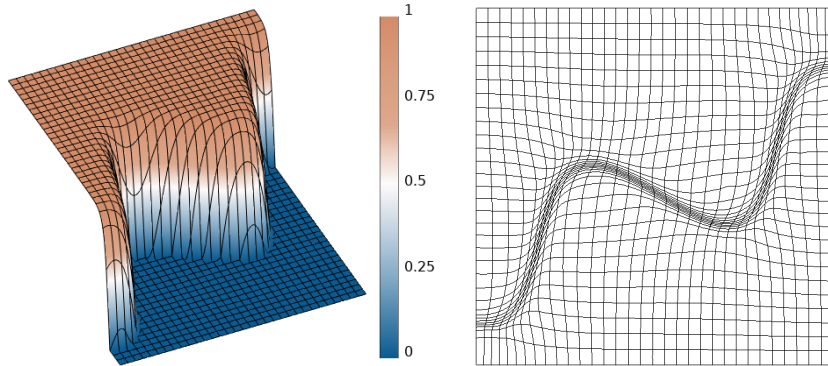


Figure 2: (left) Material indicator function on the initial uniform mesh and (right) the optimized mesh.

### 2.3. Nonlinear Solver

The optimal nodal locations are determined by minimizing the TMOP objective function (5) using the Newton’s method. At each Newton iteration, we update the nodal positions as

$$\mathbf{x}^{n+1} = \mathbf{x}^n - \alpha \Delta \mathbf{x}^n, \quad (6)$$

$$\Delta \mathbf{x}^n = [\partial^2 F(\mathbf{x}^n)]^{-1} \partial F(\mathbf{x}^n). \quad (7)$$

Here,  $\mathbf{x}^n$  refers to the vector of nodal positions at the  $n$ -th iteration during  $r$ -adaptivity,  $\alpha$  is a scalar determined by a line-search procedure, and  $\partial^2 F(\mathbf{x}^n)$  and  $\partial F(\mathbf{x}^n)$  are the Hessian and the gradient, respectively, associated with the TMOP objective function. The line-search procedure requires that  $\alpha$  is chosen such that  $F(\mathbf{x}^{n+1}) < 1.2F(\mathbf{x}^n)$ ,  $|\partial F(\mathbf{x}^{n+1})| < 1.2|\partial F(\mathbf{x}^n)|$ , and that the determinant of the Jacobian of the transformation at each quadrature point in the mesh is positive, i.e.,  $\det(A(\mathbf{x}^{n+1})) > 0$ . These line-search constraints have been tuned using many numerical experiments and have demonstrated to be effective in improving mesh quality. For Newton’s method, the Hessian  $\partial^2 F(\mathbf{x}^n)$  is inverted using the Minimum Residual (MINRES) method with Jacobi preconditioning; more sophisticated preconditioning techniques can be found in [34]. Additionally, the optimization solver iterations (6) are repeated until the relative  $l_2$  norm of the gradient of the objective function with respect to the current and original mesh nodal positions is below a certain tolerance  $\varepsilon$ , i.e.,  $|\partial F(\mathbf{x})|/|\partial F(\mathbf{x}_0)| \leq \varepsilon$ . We set  $\varepsilon = 10^{-10}$  for the results presented in the current work.

### 3. Partial Assembly for Adaptive Mesh Optimization

Traditionally, linear FEM operators are assembled and stored in the form of sparse matrices, and their action is computed using matrix-vector products. This approach can become prohibitively expensive when the polynomial degree  $p$  of the basis functions is high, as operator storage, assembly, and evaluation, per element, scale as  $\mathcal{O}(p^{2d})$ ,  $\mathcal{O}(p^{3d})$ , and  $\mathcal{O}(p^{2d})$ , respectively [8]. In contrast to this full-assembly approach, the high-order finite element community has demonstrated that using a tensor-product structure for the basis functions and integration rule with a matrix-free approach [8, 35, 3] reduces the computational complexity of FEM operators such that the storage, assembly, and evaluation, per element, scale

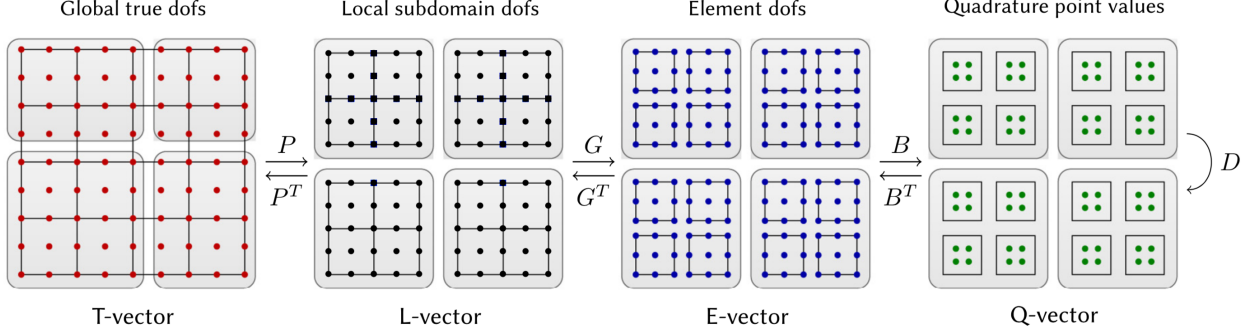


Figure 3: Fundamental finite element operator decomposition, see [8, 1].

as  $\mathcal{O}(p^d)$ ,  $\mathcal{O}(p^d)$ , and  $\mathcal{O}(p^{d+1})$ , respectively. In this section, we present our approach to extend the notion of partial assembly for FEM operators to mesh optimization.

The PA technique utilizes heavily the fundamental finite element operator decomposition [8, 1], namely, that any parallel FE operator  $A$  can be decomposed as:

$$A = P^T G^T B^T D B G P, \quad (8)$$

see Figure 3, where  $P$  represents the subdomain restriction operator that maps the global MPI vector (T-vector) to its local processor values (L-vector),  $G$  represents the element restriction operator that maps the L-vector to its element values (E-vector),  $B$  represents the basis evaluator that interpolates an E-vector to the quadrature points inside each element (Q-vector), and finally  $D$  is the operator that defines the quadrature-level computations. The idea of PA is to compute and store only the result of  $D$ , and evaluate the actions of  $P, G$  and  $B$  on-the-fly. Furthermore, PA takes advantage of the tensor product structure of the degrees of freedom and quadrature points on quadrilateral and hexahedral elements to perform the action of  $B$  without storing it as a matrix, as shown later.

In the following subsections we will often refer to the individual components of the position  $x = x(\bar{x})$ , namely,  $x = (x_1, \dots, x_d)^T$  where  $d$  is the dimension and each component is expanded as  $x_a(\bar{x}) = \sum_{i=1}^{N_x} x_{a,i} \bar{w}_i(\bar{x})$ ,  $a = 1, \dots, d$ . Then the discrete vector that contains all nodal positions is  $\mathbf{x} = \{x_{a,i}\}$  for all  $a = 1, \dots, d$  and  $i = 1, \dots, N_x$ . At places we will also redirect the interested reader to the source code of our implementation. We use the finite element library MFEM [8], specifically version 4.3.

### 3.1. Basis Functions and Tensor Products

Recall that we represent the mesh positions by (1), where on the reference element we use the scalar basis functions  $\{\bar{w}_i\}_{i=1}^{N_p}$ . For quadrilateral and hexahedral elements, we utilize basis functions that are constructed as tensor products of the standard 1D Lagrange polynomials, e.g., for  $d = 3$  we can write:

$$\bar{w}_i(\bar{x}) = \bar{w}_{i_1, i_2, i_3}(\bar{x}_1, \bar{x}_2, \bar{x}_3) = \ell_{i_1}(\bar{x}_1) \ell_{i_2}(\bar{x}_2) \ell_{i_3}(\bar{x}_3), \quad (9)$$

where  $\bar{x} = (\bar{x}_1, \bar{x}_2, \bar{x}_3)$  is a position in reference space and  $\ell_j$  denotes a 1D Lagrange polynomial (or basis function) in  $[0, 1]$  of degree  $p$ . There are  $p + 1$  such basis functions, and we will often refer to this number as  $n_i = p + 1$ . For simplicity of notation, we will identify the multi-index  $i = (i_1, i_2, i_3)$  with a single index  $i$  given by an explicit formula depending on the ordering. For example, for 3D lexicographic ordering,

$$i = 1 + (i_1 - 1) + (i_2 - 1)(p + 1) + (i_3 - 1)(p + 1)^2, \quad i_1, i_2, i_3 \in \{1, \dots, p + 1\}.$$

With the tensor-product decomposition (9), the spatial derivatives of the reference basis functions can be written as

$$\frac{\partial \bar{w}_i(\bar{x})}{\partial \bar{x}_1} = \ell'_{i_1}(\bar{x}_1) \ell_{i_2}(\bar{x}_2) \ell_{i_3}(\bar{x}_3), \quad \frac{\partial \bar{w}_i(\bar{x})}{\partial \bar{x}_2} = \ell_{i_1}(\bar{x}_1) \ell'_{i_2}(\bar{x}_2) \ell_{i_3}(\bar{x}_3), \quad \frac{\partial \bar{w}_i(\bar{x})}{\partial \bar{x}_3} = \ell_{i_1}(\bar{x}_1) \ell_{i_2}(\bar{x}_2) \ell'_{i_3}(\bar{x}_3).$$

In addition, we always use quadrature rules that are constructed from products of 1D quadrature rules. More specifically, suppose we use a quadrature rule with  $n_q$  quadrature points in each direction, having a total of  $N_q = n_q^d$  points in each element. Then a 3D quadrature point  $\chi_q$  for  $q = (q_1, q_2, q_3)$  can be represented as

$$\chi_q = \chi_{q_1, q_2, q_3} = (\chi_{q_1}, \chi_{q_2}, \chi_{q_3}),$$

where  $\{\chi_j\}$  for  $j = 1, \dots, n_q$  are the points of the 1D (e.g. Gaussian) rule. When both the basis functions and the quadrature rule have tensor product structure, we can use tensor contractions to transfer data between degrees of freedom and quadrature points, leading to efficient finite element calculations as described in the following sections.

Once a quadrature rule is selected, we define 1D reference matrices of size  $n_q \times n_i$ :

$$B_{qi}^{1D} = \ell_i(\chi_q), \quad G_{qi}^{1D} = \ell'_i(\chi_q), \quad i = 1, \dots, n_i, \quad q = 1, \dots, n_q, \quad (10)$$

where  $\ell_i$  is a 1D basis function and  $\chi_q$  is a quadrature point of the 1D quadrature rule.

### 3.2. Quadrature Level Calculations

The primary calculation at a quadrature point is that of the Jacobian matrix  $A$ , see (3). For a reference point  $\bar{x}$  the entries of  $A = A(\bar{x})$  can be written as:

$$A_{ab} = \frac{\partial x_a}{\partial \bar{x}_b} = \sum_{i=1}^{N_p} x_{a,i} \frac{\partial \bar{w}_i(\bar{x})}{\partial \bar{x}_b}, \quad a, b = 1, \dots, d.$$

Since a given element contains  $\mathcal{O}(p^d)$  degrees of freedom (DOFs) and  $\mathcal{O}(p^d)$  quadrature points, computing  $A$  at all quadrature points would be of complexity  $\mathcal{O}(p^{2d})$  assuming we precompute and store the terms  $\partial \bar{w}_i(\boldsymbol{\xi}_q)/\partial \bar{x}_b$ . When we utilize 1D tensor contractions, the entries of  $A_{ab}$  at all quadrature points in the element can be computed by (example for the 3D case when  $b = 2$ ):

$$A_{a2}(\boldsymbol{\chi}_q) = \left( \sum_{i_1} B_{q_1, i_1}^{1D} \left( \sum_{i_2} G_{q_2, i_2}^{1D} \left( \sum_{i_3} B_{q_3, i_3}^{1D} x_{a, i_1, i_2, i_3} \right) \right) \right) = [B^{1D} \otimes G^{1D} \otimes B^{1D} \mathbf{x}_{E,a}]_{q_1, q_2, q_3}$$

where  $\mathbf{x}_{E,a} = \{x_{a,i}\}_{i=1}^{N_p}$ . Here the  $\otimes$  symbol denotes the tensor outer product which means that the matrices will be applied as a sequence of multiplications as given by the above formula. The important point here is that each contraction is of complexity  $\mathcal{O}(p^{d+1})$  (as  $\mathbf{x}_{E,a}$  is a tensor of rank  $d$ ), resulting in an overall complexity of  $\mathcal{O}(p^{d+1})$ . This is a significant improvement over  $\mathcal{O}(p^{2d})$ , especially for high  $p$ . One complication with tensor contractions is that the implementation has to take care of arranging the vectors  $\mathbf{x}_E$  in a suitable tensor form.

The rest of the quadrature level calculations are independent of the finite element discretization, i.e., they do not involve the finite element basis functions  $\{\bar{w}_i\}$ . Here the notion of sum factorization does not apply; computational gains can be achieved on GPU devices by proper batching over many quadrature points. The major quadrature level calculations are the following:

- Given physical coordinates of a point  $x$ , construct the target matrix  $W(x)$  and compute  $\det(W(x))$ . In the case of adaptivity, additional simulation-specific values also provided as input to the computation of  $W$ .
- Given a  $d \times d$  matrix  $T$ , compute the mesh quality metric the  $\mu(T)$ , its first derivative

$\partial\mu/\partial T$  which is a  $d \times d$  matrix, and its second derivative  $\partial^2\mu/\partial T^2$  which is a  $d \times d \times d \times d$  tensor. These are derived using standard matrix algebra, e.g. [36].

### 3.3. Objective Function and First Derivative

In this section we consider the TMOP objective function of the form (5) and its first derivative. In this section we focus on the first term in (5) while the second term will be discussed later in Section 3.5.

To evaluate the objective function  $F(\mathbf{x})$  one can use the following decomposition similar to (8)

$$F(\mathbf{x}) = \mathbf{1}^T D_0(BGP\mathbf{x})$$

where  $\mathbf{1}$  is a vector of ones and  $D_0$  evaluates, at all quadrature points, the integrand of the first term in (5) after changing the variables in the integral from  $E_t$  to  $\bar{E}$  and applying the quadrature rule:

$$D_0(A) = w_q \det(W) \omega(x_t) \mu(AW^{-1}). \quad (11)$$

Here  $w_q$  is the quadrature point weight,  $\omega(x_t) \det(W)$  and  $W$  are the precomputed values for the current quadrature point, and  $A$  is the Jacobian matrix at the current quadrature point computed by evaluating  $BGP\mathbf{x}$ .

The main speedup in the calculation of the objective function comes from proper batching of the computation of the Jacobian  $A$  over all quadrature points, as explained in Section 3.2. Once  $T = AW^{-1}$  and  $\mu(T)$  are computed at all quadrature points, the final integral is readily available.

The computation of the gradient  $\partial F/\partial \mathbf{x}$  is improved by utilizing the PA technique. For simplicity, in the formulas below we assume that  $W = I$  (the target elements coincide with the reference one), although this is generally not the case as explained in Section 3.6. Then the first derivative of the objective  $F$  with respect of the node  $x_{a,i}$  for each element is:

$$\begin{aligned} \frac{\partial F(\mathbf{x})}{\partial x_{a,i}} &= \int_{\bar{E}} \frac{\partial \mu}{\partial T(\mathbf{x})} : \frac{\partial T(\mathbf{x})}{\partial x_{a,i}} d\bar{x} = \int_{\bar{E}} \frac{\partial \mu}{\partial T} : \left( \frac{\partial A}{\partial x_{a,i}} \right) d\bar{x} \\ &= \sum_{q=1}^{N_q} z_q \left[ \sum_{m,n=1}^d \frac{\partial \mu}{\partial T_{mn}} \delta_{m,a} \frac{\partial \bar{w}_i(\mathbf{x}_q)}{\partial \bar{x}_n} \right], \quad a = 1, \dots, d, \quad i = 1, \dots, N_x, \end{aligned} \quad (12)$$

where  $z_q$  is the quadrature point weight and  $\delta$  is the standard Kronecker delta. The dependence of  $x$  in (12) comes through the nonlinearity of  $\mu(T)$ . With PA we efficiently compute

all quadrature points together, as a result of a tensor contraction. We first form a  $D$  matrix of size  $n_q \times n_q \times n_q$  in each element that stores all quadrature data, e.g., the derivatives  $\partial\mu/\partial T$ . This quadrature-based calculation is of complexity  $\mathcal{O}(p^d)$ . Then  $D, \mathbf{x}, B, G$  are contracted appropriately to obtain the final derivative vector, with complexity  $\mathcal{O}(p^{d+1})$ . These contraction calculation are complicated and can be found in the mfem-4.3 source in files `fem/tmop/tmop_pa_p2.cpp` and `fem/tmop/tmop_pa_p3.cpp` for 2D and 3D, respectively. Once the gradient of the TMOP objective function is computed on an element-by-element basis (E-vector), it is mapped to a global T-vector, see Figure 3, to ensure that the gradients are consistent for DOFs that are shared between neighboring elements.

### 3.4. Second Derivative and Linear Solver

Again assuming  $W = I$ , the second derivative of  $F$  for the nodes  $x_{a,i}$  and  $x_{b,j}$  is:

$$\begin{aligned} \frac{\partial^2 F(\mathbf{x})}{\partial x_{b,j} \partial x_{a,i}} &= \int_{\bar{E}} \frac{\partial}{\partial x_{b,j}} \left[ \frac{\partial \mu}{\partial T} : \left( \frac{\partial A}{\partial x_{a,i}} \right) \right] d\bar{x} \\ &= \sum_{q=1}^{N_q} z_q \left[ \sum_{m,n=1}^d \sum_{o,p=1}^d \frac{\partial^2 \mu}{\partial T_{op} \partial T_{mn}} \delta_{o,b} \frac{\partial \bar{w}_j(\chi_q)}{\partial \bar{x}_p} \delta_{m,a} \frac{\partial \bar{w}_i(\chi_q)}{\partial \bar{x}_n} \right], \quad (13) \\ a, b &= 1, \dots, d, \quad i, j = 1, \dots, N_x, \end{aligned}$$

where  $z_q$  is the quadrature point weight and  $\delta$  is the standard Kronecker delta. Assembling and applying the Hessian matrix  $\partial^2 F$  are the two most expensive computations in our algorithm. The classical (full assembly) approach forms a sparse matrix over all DOFs in the problem, requiring to store  $\mathcal{O}(p^{2d})$  entries per element. Computing these entries with standard nested loops requires  $\mathcal{O}(p^{3d})$  operations per element, while applying the sparse matrix to a vector is complexity  $\mathcal{O}(p^{2d})$ . Since  $\partial^2 F$  depends on the current mesh positions (due to the nonlinearity of  $\mu$  with respect to  $T$ ), the assembly must be performed at every Newton iteration. For higher mesh orders  $p$  these computations become prohibitively expensive, especially in 3D.

The use of PA for  $\partial^2 F$  is critical, as it avoids the formation of a global sparse matrix. In this case the assembly is replaced by pre-computing and storing the quadrature-specific data at all quadrature points, with complexity and storage of  $\mathcal{O}(p^d)$  per element. The action of  $\partial^2 F$  is performed element-by-element, using tensor contractions involving the quadrature

data, the DOF vector  $\mathbf{x}$ , and the 1D matrices  $B$  and  $G$ . This PA-based action is of complexity  $\mathcal{O}(p^{d+1})$  per element. The complete calculation can be seen in mfem-4.3's source files `fem/tmop/tmop_pa_h2m.cpp` and `fem/tmop/tmop_pa_h3m.cpp` for 2D and 3D, respectively. The assembly of all quadrature point data is in the files `fem/tmop/tmop_pa_h2s.cpp` and `fem/tmop/tmop_pa_h3s.cpp` for 2D and 3D, respectively. The inversion of  $\partial^2 F$  is performed by an iterative solver that uses the PA-based action of the operator. Our default choice is the Minimum Residual (MINRES) method, as  $\partial^2 F$  is symmetric but not necessarily positive-definite. Preconditioning for matrix-free inversion is a substantial challenge and an active area of research [5]. We have the option to perform Jacobi preconditioning, as the diagonal of  $\partial^2 F$  can be computed through tensor contractions without having the global matrix; these algorithms can be found in files `fem/tmop/tmop_pa_h2d.cpp` and `fem/tmop/tmop_pa_h3d.cpp` for 2D and 3D, respectively.

### 3.5. Limiting of Node Displacements

The term involving the limiting function  $\xi(x - x_0, \delta(x_0))$  in (5) is used to restrict the node displacements in certain regions of the domain during mesh optimization, see Section 3.2 of [7]. A simple example of a node limiting function is  $\xi(x - x_0, \delta(x_0)) = (x - x_0)^2 / \delta^2$ , which would start to dominate the objective function once the displacements go above the local  $\delta$  value. Computing this term and its derivatives through PA does not present any difficulty. For example, the second derivative of this term is:

$$\begin{aligned} \frac{\partial^2}{\partial x_{b,j} \partial x_{a,i}} \int_{E_t} \xi(x - x_0, \delta(x_0)) dx_t &= \int_{\bar{E}} \det(W) \frac{\partial^2 \xi}{\partial x_b \partial x_a} \frac{\partial x_b}{\partial x_{b,j}} \frac{\partial x_a}{\partial x_{a,i}} d\bar{x} \\ &= \sum_{q=1}^{N_q} z_q \det(W(\bar{x}_q)) \frac{\partial^2 \xi}{\partial x_b \partial x_a} \bar{w}_j(\bar{x}_q) \bar{w}_i(\bar{x}_q), \end{aligned} \quad (14)$$

which resembles a standard FE mass operator. Dependence on the current mesh positions  $x$  in (14) appears when  $\xi$  is chosen as a nonlinear function with respect to  $x - x_0$ . The PA-based action is formed by contracting  $B$  and  $\mathbf{x}$  with the matrix  $D$  that contains all the quadrature data needed in (14). For example, in 3D, the action of this operator to a vector  $\mathbf{x}$  (rearranged as a tensor  $X$ ) is computed as

$$B^{1D^T} \otimes B^{1D^T} \otimes B^{1D^T} \otimes D \otimes B^{1D} \otimes B^{1D} \otimes B^{1D} X.$$

The implementation of the above computation can be found in the following mfem-4.3 source files: `fem/tmop/tmop_pa_h2m_c0.cpp` and `fem/tmop/tmop_pa_h3m_c0.cpp` for 2D and 3D, respectively.

### 3.6. Adaptivity and Field Transfer

When TMOP is used to achieve r-adaptivity, the definitions of the target matrices contain information about discrete simulation fields [7]. For illustration purposes, we denote such simulation fields by  $\eta(x)$ , which for our purposes is always a FE function. The evaluation of  $W$  requires the evaluation of  $\eta(x)$ , which is optimized by tensor contractions, that is, the  $\eta$  values at all quadrature points are obtained through  $d$  contractions of the  $B^{1D}$  matrices.

The target matrices  $W$  becomes space-dependent through its  $\eta$  dependence. Since  $\partial W / \partial x \neq 0$ , the derivatives in equations (12), (13) and (14) become more complicated, as well as their PA implementation. In our experience, adding the extra derivative terms does not change the results in a significant way, and we don't include these terms in our current implementation. The dependence of  $W$  on  $x$  is still accounted by the algorithm, as the targets are recomputed after every position change in the nonlinear iteration.

Since finite element fields are only defined with respect to the initial mesh  $\mathcal{M}_0$ , remap procedures are needed to obtain their values on the different meshes obtained during the mesh optimization iterations [32, 37]. Our GPU implementation utilizes the so-called advection approach, where remap is achieved by solving an advection PDE in pseudo-time. This approach is entirely based on standard finite element operations, enabling the use of sum factorization and optimized matrix-free kernels. By defining a mesh velocity  $v = x - x_0$ , the remap of a function  $\eta(x)$  is posed as the following PDE in pseudo-time  $\tau \in [0, 1]$ :

$$\frac{d\eta(x_\tau, \tau)}{d\tau} = v \cdot \nabla \eta(x_\tau, \tau), \quad x_\tau = x_0 + \tau v, \quad \eta(x_0, 0) = \eta_0(x_0).$$

More details about the mathematical formulation can be found in Section 4.2 of [32]. Solving the above PDE in a matrix-free manner requires to define the actions of a mass operator and an advection operator. The mass operator is applied many times per time step, as it is used by a conjugate gradient linear solver. The advection operator is applied once per time step, to form the right-hand-side of the linear system. The actions of these operators are standard FE kernels, and we directly use their optimized PA implementations from MFEM.

## 4. Numerical Results

In this section we present several numerical examples and benchmarks demonstrating the improvement in computational efficiency due to use of partial assembly on GPU-based architectures in comparison to full-assembly on CPUs.

### 4.1. Kershaw Benchmark

Below we propose a performance benchmark for optimization of high-order meshes. The setup is based on the Kershaw meshes introduced in [38]. The test is designed so that both the initial (deformed) mesh and the final (optimized) mesh are straightforward to reproduce. This allows to compare the performance of different optimization methods on a problem with well-defined initial configuration and final output.

The initial mesh (that will be optimized) is obtained by an analytic deformation of a uniform Cartesian mesh. The deformation curves and distorts the elements, allowing to quantify the performance of the method in terms of speed and accuracy for meshes of different orders and element counts. The Kershaw meshes [38, 39] are parameterized by two anisotropy parameters  $\varepsilon_y, \varepsilon_z \in (0, 1]$  such that the meshes are uniform for  $\varepsilon_y = \varepsilon_z = 1$  and become increasingly anisotropic as  $\varepsilon_y$  and  $\varepsilon_z$  decrease, see Figure 4. To obtain the Kershaw mesh, the  $x$ -axis of the mesh is decomposed into 6 equally sized layers, and elements in the leftmost and rightmost layers are modified to have aspect-ratios  $1/\varepsilon_y$  and  $1/\varepsilon_z$ . The high aspect-ratio elements are placed in the opposite corners, while the intermediate layers are smoothly transitioned with a piecewise quintic function. The generating C++ code is provided in Appendix A for convenience. Due to the problem setup, the number of elements in the  $x$ -direction must be an integer multiple of 6, while in the  $y$ - and  $z$ -directions must be multiples of 2.

*Baseline Wall Time.* First we report baseline time-to-solution for a complete mesh optimization computation, that is, evolving an initially deformed mesh to the ideal uniform configuration. The deformed meshes are obtained by  $\varepsilon_y = \varepsilon_z = 0.3$  and the resolution is fixed to  $24 \times 24 \times 24$ . We present timings for different mesh orders, different solver strategies (Newton’s method with and without preconditioner), and different architectures (CPU versus GPU). For these experiments, the quadrature order is fixed at 8, resulting in  $9^3$  quadrature

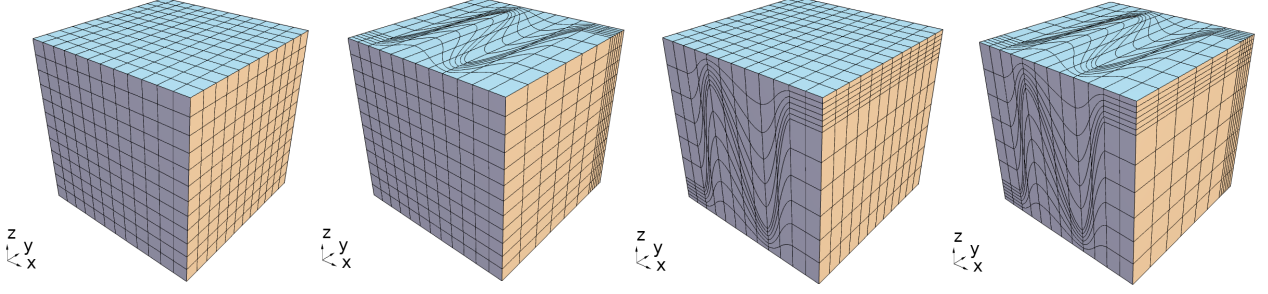


Figure 4: Kershaw meshes: (left to right) (a)  $\varepsilon_y = \varepsilon_z = 1$ , (b)  $\varepsilon_y = 0.3$ ,  $\varepsilon_z = 1$ , (c)  $\varepsilon_y = 1$ ,  $\varepsilon_z = 0.3$ , and (d)  $\varepsilon_y = \varepsilon_z = 0.3$ .

points per element, maximum number of linear solver iterations per Newton iterations is 60, and  $\mu_{303} = \frac{|T|^2}{3\tau^{(2/3)}} - 1$  is used for shape optimization. The results presented here were obtained on Lassen, a Livermore Computing supercomputer, that has IBM Power9 CPUs (792 nodes with 44 CPU cores per node) and NVIDIA V100 GPUs (4 per node). All reported computations utilize a single machine node. The CPU runs use 36 CPU cores, while the GPU runs utilize 4 CPU cores with 1 GPU per core.

Table 1 compares the unique degrees of freedom and total quadrature points per core, total time to solution, Newton iterations, and MINRES iterations, for different mesh orders ( $p = 1, \dots, 4$ ) and different solver strategies. The corresponding data is also shown in Figure 5. We note that the use of GPUs leads to a 30-40 $\times$  speed up in comparison to CPUs. We also quantify the total time spent in each of the main kernels (gradient, Hessian, etc.) during mesh optimization in Figure 6.

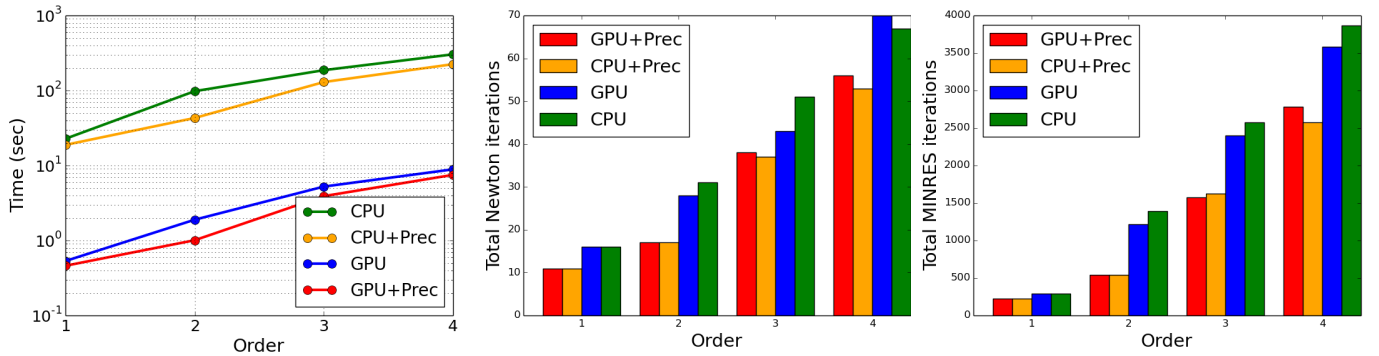


Figure 5: (left to right) Comparison of (a) total time to solution, (b) Newton iterations, and (c) MINRES iterations for different solver strategies and architectures.

	Unique Degrees of Freedom			
	$p = 1$	$p = 2$	$p = 3$	$p = 4$
	46,875	352,947	1,167,051	2,738,019
	Quadrature points per core ( $\frac{E(Q+1)^d}{P}$ )			
CPU	279,936			
GPU	2,519,424			

(a)

	Total Newton Iterations			
	$p = 1$	$p = 2$	$p = 3$	$p = 4$
CPU	16	31	51	67
CPU+Prec	11	17	37	53
GPU	16	28	43	70
GPU+Prec	11	17	38	56

(c)

	Time to solution (sec)			
	$p = 1$	$p = 2$	$p = 3$	$p = 4$
CPU	22.7	97.9	186.7	303.4
CPU+Prec	18.8	43.0	129.6	224.3
GPU	0.5	1.9	5.2	8.9
GPU+Prec	0.4	1.0	3.9	7.5
	Speedup (GPU+Prec vs CPU+Prec)			
	<b>47×</b>	<b>43×</b>	<b>33×</b>	<b>30×</b>

(b)

	Total MINRES Iterations			
	$p = 1$	$p = 2$	$p = 3$	$p = 4$
CPU	293	1395	2577	3869
CPU+Prec	227	539	1621	2574
GPU	295	1216	2397	3586
GPU+Prec	227	539	1572	2781

(d)

Table 1: For meshes of different orders ( $p$ ), we compare (a) unique degrees of freedom and total quadrature points per core, (b) total time to solution, (c) total Newton iterations, and (d) total MINRES iterations.

*Strong scaling.* A strong scaling study of the GPU algorithm is reported in Figure 7 on up to 128 GPUs. For all computations, the number of elements is fixed to  $96 \times 96 \times 96$ . For ideal strong scaling, the time per cycle would decrease linearly as we increase the GPU count. As expected, the scaling deteriorates as the GPU count increases, as there is no longer sufficient work to feed each GPU.

Every data point in Figure 7 is obtained by timing the computation of a single Newton iteration on the initial deformed mesh, with 20 iterations of the MINRES linear solver. The number of quadrature point per element is set to  $3^3, 4^3, 5^3$ , and  $6^3$  for mesh orders 1, 2, 3, and 4, respectively.

*Throughput.* Next we provide throughput results that demonstrate how well the proposed algorithms utilize the machine resources as the problem size increases. The plots on Figure

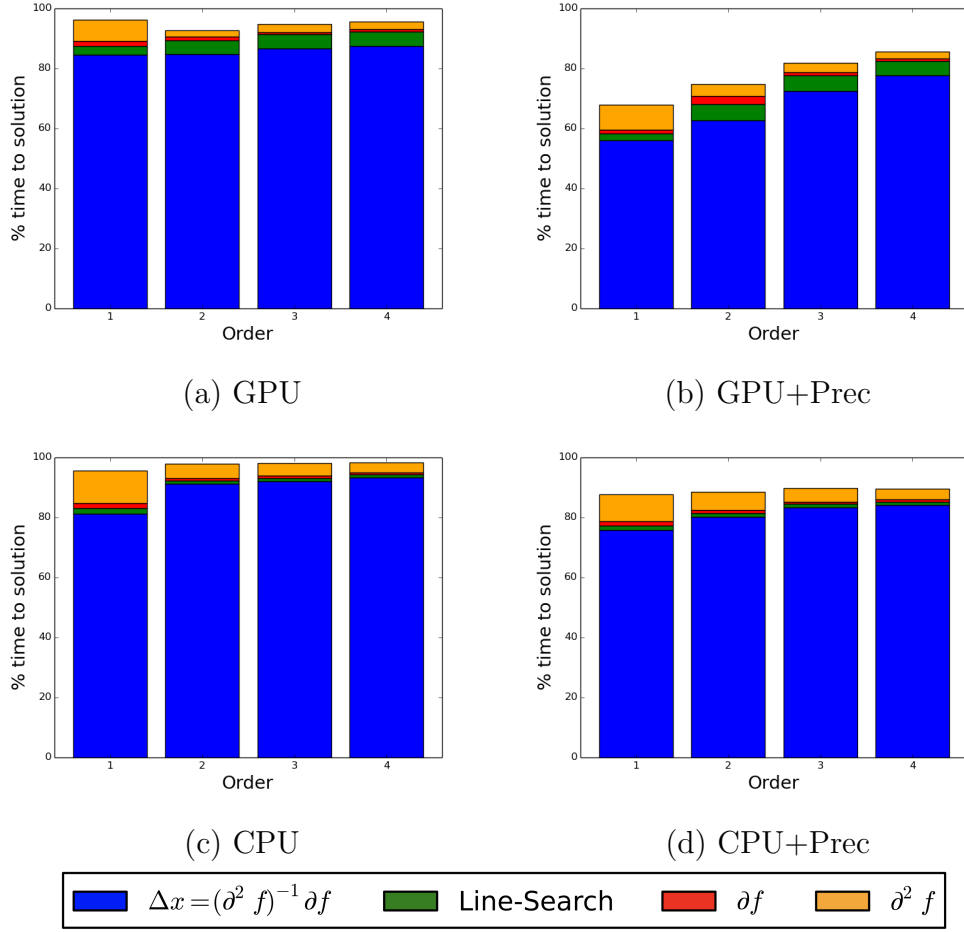


Figure 6: Percentage of the total time spent in different Kernels for different solver strategies and architectures.

8 show the throughput for our most important kernel, i.e., the action of  $\partial^2 F$ , in terms of billions of degrees of freedom processed per second vs. the problem size in the CPU and GPU cases. Such plots are useful in comparing the performance of different orders and problem size in both the weak and scale limits, see e.g. [1]. For example, higher throughput means faster run time, and from Figure 8 we can see that on both platforms higher orders perform better, but the difference is much more significant on GPUs. Furthermore, while CPU performance is relatively flat across problem sizes, the GPU requires significant number of unknowns (in the millions of degrees of freedom) to achieve the best results.

Figure 9 shows the throughput for the complete TMOP algorithm for a single GPU. Again we observe that the higher orders achieve better computational intensity, especially for larger problems. Every data point in Figures 8 and 9 is obtained by timing the computation of a

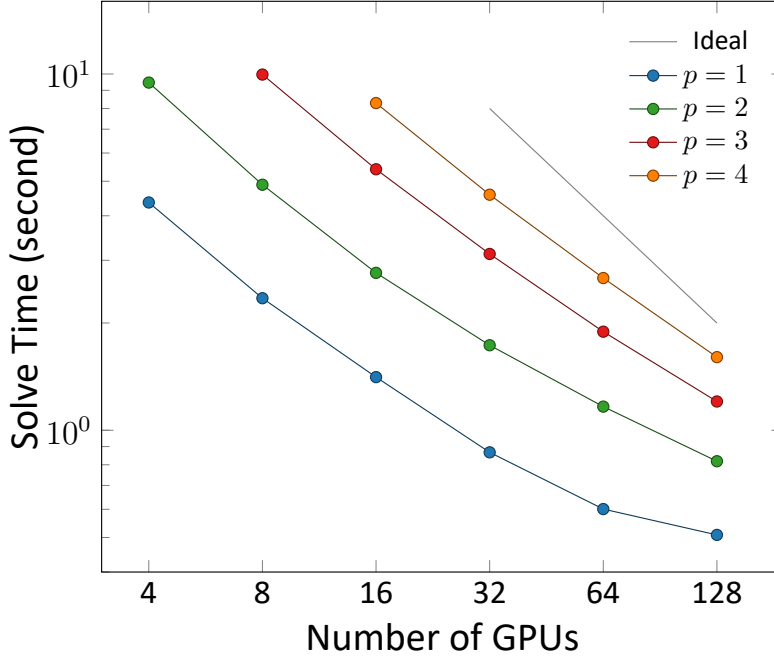


Figure 7: Strong scaling for the Kershaw benchmark.

single Newton iteration on the initial deformed mesh. The number of linear solver iteration is fixed to 20 to make sure every data point represents the same amount of computational work. The number of quadrature point per element is set to  $3^3$ ,  $4^3$ ,  $5^3$ , and  $6^3$  for mesh orders 1, 2, 3, and 4, respectively.

#### 4.2. ALE Simulation with Material-Adaptive TMOP

In this section we demonstrate the proposed GPU-algorithms in the settings of a multimaterial ALE hydrodynamics production code. We consider a simulation of the BRL81a shaped charge using the MARBL multiphysics application [40]. A shaped charge is a device which focuses the pressures of a high explosive onto a metal “liner” to form a hyper-velocity jet which can be used in many applications, including armor penetration, metal cutting and perforation of wells for the oil/gas industry [41].

The ALE hydrodynamics algorithm consists of the following phases:

1. High-order Lagrange multimaterial hydrodynamics on a moving, unstructured, high-order mesh [42], including use of GPU accelerated 3rd party libraries for material

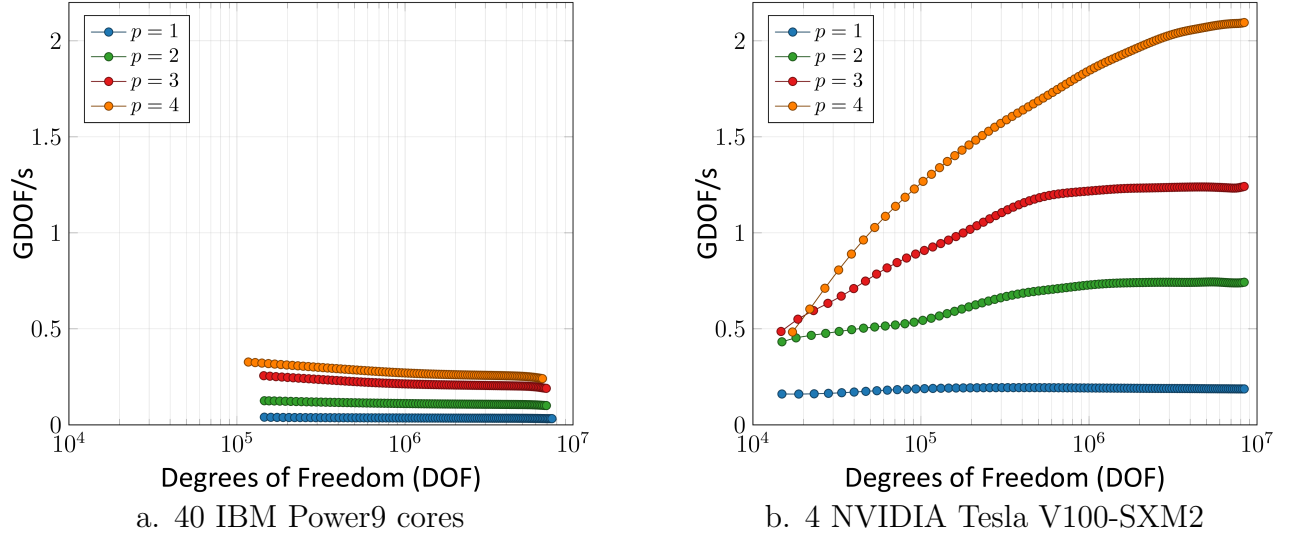


Figure 8: Throughput comparison - action of the second derivative operator. Single Lassen node throughput (in GDOF/s, i.e. billions of degrees of freedom per second) of (a) 40 IBM Power9 CPU cores and (b) 4 NVIDIA Tesla V100-SXM GPU.

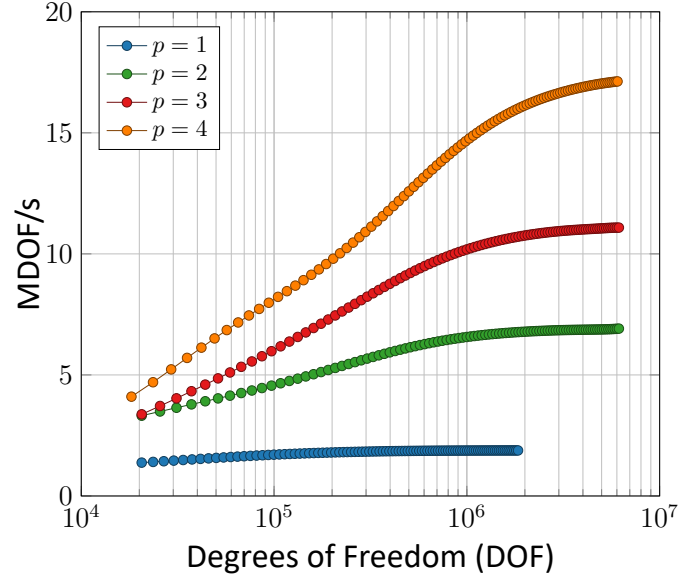


Figure 9: Throughput of the complete TMOP computation. Single NVIDIA Tesla V100-SXM GPU throughput (in MDOF/s, i.e. millions of processed degrees of freedom per second).

equations of state (EOS) evaluation and material constitutive models.

2. Non-linear, material adaptive, high-order mesh optimization using the presented TMOP method.

3. High-order continuous (kinematic) and discontinuous Galerkin (thermodynamic) advection-based remap using flux corrected transport (FCT).

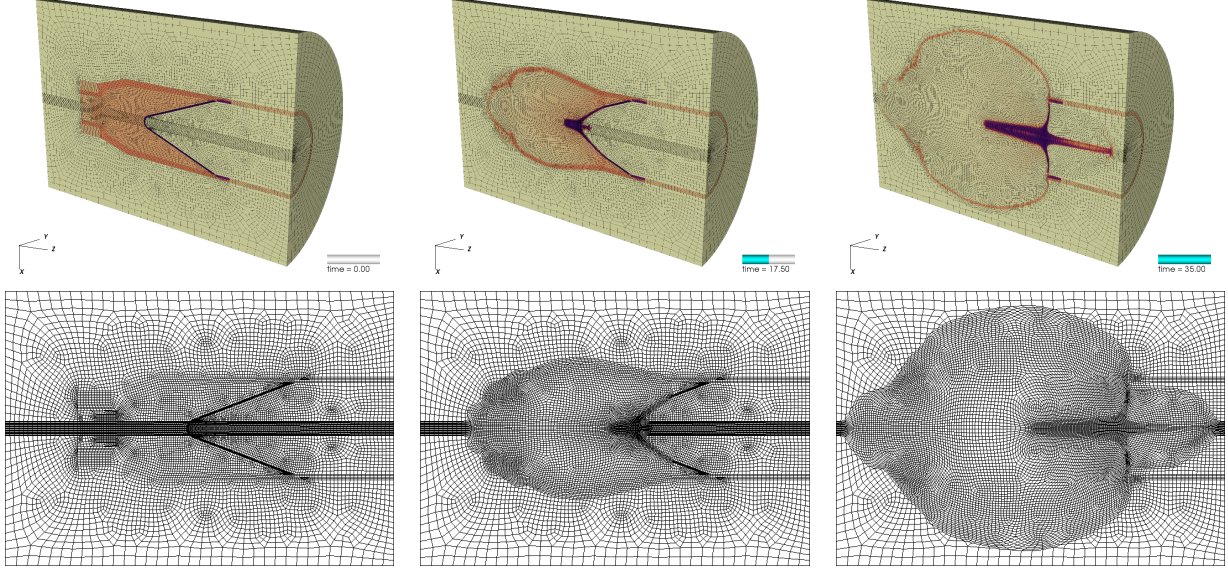


Figure 10: Snapshots of the density (*top*) and mesh (*bottom*) for the ALE shaped charge GPU simulation using material adaptive TMOP at times  $t=0$ , 17.5 and 35 (*left to right*).

In Figure 10, we show results of a MARBL calculation of the BRL81a model with all three phases of the ALE algorithm run on the GPU. To enhance the high-order mesh resolution near the hyper-velocity copper jet, we employ the material adaptive capabilities of the TMOP mesh optimization phase at the copper material with a 2:1 size ratio. To prevent the mesh from moving in regions which have not experienced hydrodynamic motion, we utilize the limiting term in our optimization metric. We use  $p = 2$  elements for the mesh and the continuous kinematic fields with 64 quad points per element (combined with  $p = 1$  DG elements for the thermodynamic variables). This simulation consists of 14,346,240 total quadrature points on a high-order ( $p = 2$ ), highly unstructured mesh. We run the problem using 2 nodes of the Lassen machine at LLNL and compare performance results between the CPU only case (80 IBM Power9 cores) and the GPU case (8 NVIDIA Tesla V100-SXM GPUs) for total of 2500 simulation cycles. Over these 2500 cycles, the code performs ALE remap at fixed time intervals for a total of 25 ALE steps. The material adaptive TMOP Newton solver is run at each ALE step with an outer residual tolerance of  $10^{-10}$  with a max of 10 iterations while the inner linear solver has a max of 100 iterations. The relative

performance comparison between the CPU and GPU node simulations is shown in Table 2 and Table 3. In the CPU case, mesh optimization takes a substantially larger portion of the overall runtime, comprising 15% of total wall time vs. 7% in the GPU case as shown in Table 2. The GPU speedup for the mesh optimization phase of the simulation is over  $20\times$  as shown in Table 3.

	Lagrange	Mesh Optimization	Remap	Other
CPU	31.34%	14.86%	53.53%	0.17%
GPU	14.00%	6.72%	73.39%	5.89%

Table 2: Percentage of total run time for each phase of the multimaterial ALE simulation. Comparison of CPU vs GPU runs.

	Min time/rank	Max time/rank	Avg time/rank	Speedup
CPU MeshOpt	4730.828	4730.831	4730.830	-
CPU Action	4713.425	4713.427	4713.426	-
GPU MeshOpt	288.126	289.125	288.842	<b><math>16.37\times</math></b>
GPU Action	209.422	209.436	209.430	<b><math>22.51\times</math></b>

Table 3: Total run time with min/max/avg time across all MPI ranks (80 for CPU, 8 for GPU) for the full mesh optimization phase (MeshOpt) and for the  $\partial^2 F$  operator evaluation (Action) over 2500 simulation cycles for the multimaterial ALE simulation. Comparison of CPU vs GPU runs.

## 5. Conclusion

This paper discussed the use of finite element partial assembly techniques in the context of high-order mesh optimization. We demonstrated that this approach leads to substantial improvements in performance complexity for tensor-product elements (quads and hexes), and the resulting tensor contractions perform well on GPU hardware. In addition, we proposed a simple mesh optimization benchmark for the mesh optimization community. Our method relies on efficient matrix-free preconditioning, which is still an area of active research. We plan to explore that further in a future publication.

## References

- [1] T. V. Kolev, P. Fischer, M. Min, J. Dongarra, J. Brown, V. Dobrev, T. Warburton, S. Tomov, M. Shephard, A. Abdelfattah, V. Barra, N. Beams, J.-S. Camier, N. Chalmers, Y. Dudouit, A. Karakus, I. Karlin, S. Kerkemeier, Y.-H. Lan, D. Medina, E. Merzari, A. Obabko, W. Pazner, T. Rathnayake, C. Smith, L. Spies, K. Świrydowicz, J. Thompson, A. Tomboulides, V. Z. Tomov, Efficient exascale discretizations: High-order finite element methods, *Int. J. High Perform. Comput. Appl.* (2021). doi: 10.1177/10943420211020803. 1, 2, 8, 18
- [2] V. A. Dobrev, P. Knupp, T. V. Kolev, K. Mittal, V. Z. Tomov, The Target-Matrix Optimization Paradigm for high-order meshes, *SIAM J. Sci. Comp.* 41 (1) (2019) B50–B68. 2, 4
- [3] M. O. Deville, P. F. Fischer, P. F. Fischer, E. Mund, et al., High-order methods for incompressible fluid flow, Vol. 9, Cambridge university press, 2002. 2, 7
- [4] P. D. Bello-Maldonado, T. V. Kolev, R. N. Rieben, V. Z. Tomov, A matrix-free hyperviscosity formulation for high-order ALE hydrodynamics, *Computers & Fluids* (2020) 104577. 2
- [5] M. Franco, J.-S. Camier, J. Andrej, W. Pazner, High-order matrix-free incompressible flow solvers with GPU acceleration and low-order refined preconditioners, *Computers & Fluids* (2020) 104541. 2, 13
- [6] M. Kronbichler, K. Kormann, Fast matrix-free evaluation of discontinuous Galerkin finite element operators, *ACM Transactions on Mathematical Software (TOMS)* 45 (3) (2019) 1–40. 2
- [7] V. A. Dobrev, P. Knupp, T. V. Kolev, K. Mittal, R. N. Rieben, V. Z. Tomov, Simulation-driven optimization of high-order meshes in ALE hydrodynamics, *Comput. Fluids* (2020). 2, 4, 13, 14
- [8] R. Anderson, J. Andrej, A. Barker, J. Bramwell, J.-S. Camier, J. Cervený, V. A. Dobrev, Y. Dudouit, A. Fisher, T. V. Kolev, W. Pazner, M. Stowell, V. Z. Tomov, I. Akkerman,

- J. Dahm, D. Medina, S. Zampini, MFEM: a modular finite elements methods library, *Comput. Math. Appl.* 81 (2020) 42–74. doi:10.1016/j.camwa.2020.06.009. 2, 7, 8
- [9] V. A. Dobrev, P. Knupp, T. V. Kolev, K. Mittal, V. Z. Tomov, HR-adaptivity for nonconforming high-order meshes with the Target-Matrix Optimization Paradigm, *Eng. Comput.* (2021). doi:10.1007/s00366-021-01407-6. 3
- [10] J. Vollmer, R. Mencl, H. Mueller, Improved Laplacian smoothing of noisy surface meshes, in: *Computer graphics forum*, Vol. 18, Wiley Online Library, 1999, pp. 131–138. 3
- [11] D. A. Field, Laplacian smoothing and Delaunay triangulations, *Communications in applied numerical methods* 4 (6) (1988) 709–712. 3
- [12] G. Taubin, et al., Linear anisotropic mesh filtering, *Res. Rep. RC2213 IBM* 1 (4) (2001). 3
- [13] P. Knupp, Introducing the target-matrix paradigm for mesh optimization by node movement, *Engr. with Comptr.* 28 (4) (2012) 419–429. 3
- [14] A. Gargallo-Peiró, X. Roca, J. Peraire, J. Sarrate, Optimization of a regularized distortion measure to generate curved high-order unstructured tetrahedral meshes, *International Journal for Numerical Methods in Engineering* 103 (5) (2015) 342–363. 3
- [15] K. Mittal, P. Fischer, Mesh smoothing for the spectral element method, *Journal of Scientific Computing* 78 (2) (2019) 1152–1173. 3
- [16] P. T. Greene, S. P. Schofield, R. Nourgaliev, Dynamic mesh adaptation for front evolution using discontinuous Galerkin based weighted condition number relaxation, *Journal of Computational Physics* 335 (2017) 664–687. 3
- [17] M. Turner, J. Peiró, D. Moxey, Curvilinear mesh generation using a variational framework, *Computer-Aided Design* 103 (2018) 73–91. 3

- [18] G. Aparicio-Estrems, A. Gargallo-Peiró, X. Roca, Defining a stretching and alignment aware quality measure for linear and curved 2d meshes, in: International Meshing Roundtable, Springer, 2018, pp. 37–55. 3
- [19] W. Huang, Y. Ren, R. D. Russell, Moving mesh partial differential equations (MM-PDES) based on the equidistribution principle, SIAM J. Numer. Anal. 31 (3) (1994) 709–730. 3
- [20] W. Huang, R. D. Russell, Adaptive moving mesh methods, Springer Science & Business Media, 2010. 3
- [21] D. An, N. Lei2B, T. Zhao, H. Si, X. Gu, A moving mesh adaptation method by optimal transport (2021). 3
- [22] J. G. Wallwork, N. Barral, D. A. Ham, M. D. Piggott, Anisotropic goal-oriented mesh adaptation in firedrake, 28th Intl Meshing Roundtable, Zenodo (2020) 83–100. 3
- [23] D. Zint, R. Grosso, F. Lunz, Discrete mesh optimization on surface and volume meshes, 28th International Meshing Roundtable. Zenodo (2020). 3
- [24] O. Coulaud, A. Loseille, Very high order anisotropic metric-based mesh adaptation in 3d, Procedia engineering 163 (2016) 353–365. 3
- [25] J. P. D’Amato, M. Vénere, A CPU–GPU framework for optimizing the quality of large meshes, Journal of Parallel and Distributed Computing 73 (8) (2013) 1127–1134. 3
- [26] D. Zint, R. Grosso, Discrete mesh optimization on GPU, in: International Meshing Roundtable, Springer, 2018, pp. 445–460. 3
- [27] J. Eichstädt, M. Green, M. Turner, J. Peiró, D. Moxey, Accelerating high-order mesh optimisation with an architecture-independent programming model, Computer Physics Communications 229 (2018) 36–53. 3
- [28] G. Mei, J. C. Tipper, N. Xu, A generic paradigm for accelerating Laplacian-based mesh smoothing on the GPU, Arabian Journal for Science and Engineering 39 (11) (2014) 7907–7921. 3

- [29] E. Shaffer, Z. Cheng, R. Yeh, G. Zagaris, L. Olson, Simple and effective GPU-based mesh optimization, *Parallel Computing: Accelerating Computational Science and Engineering (CSE)* 25 (2014) 285–294. 3
- [30] P. Fischer, M. Min, T. Rathnayake, S. Dutta, T. Kolev, V. Dobrev, J.-S. Camier, M. Kronbichler, T. Warburton, K. Swirydowicz, J. Brown, Scalability of high-performance PDE solvers, *Int. J. HPC App.* 34 (5) (2020) 562–586. doi:10.1177/1094342020915762. 3
- [31] P. Knupp, Target formulation and construction in mesh quality improvement, Tech. Rep. LLNL-TR-795097, Lawrence Livermore National Lab.(LLNL), Livermore, CA (2019). doi:10.2172/1571722.  
URL <https://www.osti.gov/biblio/1571722> 5
- [32] V. A. Dobrev, P. Knupp, T. V. Kolev, V. Z. Tomov, Towards Simulation-Driven Optimization of High-Order Meshes by the Target-Matrix Optimization Paradigm, Springer International Publishing, 2019, pp. 285–302. 5, 14
- [33] P. Knupp, Metric type in the target-matrix mesh optimization paradigm, Tech. Rep. LLNL-TR-817490, Lawrence Livermore National Lab.(LLNL), Livermore, CA (United States) (2020). doi:10.2172/1782521.  
URL <https://www.osti.gov/biblio/1782521> 6
- [34] E. Ruiz-Gironés, X. Roca, Automatic penalty and degree continuation for parallel preconditioned mesh curving on virtual geometry, *Comput.-Aided Des.* 146 (2022) 103208. doi:10.1016/j.cad.2022.103208. 7
- [35] S. A. Orszag, Spectral methods for problems in complex geometries, in: *Numerical methods for partial differential equations*, Elsevier, 1979, pp. 273–305. 7
- [36] K. B. Petersen, M. S. Pedersen, The matrix cookbook (version: November 15, 2012) (2012). 11
- [37] K. Mittal, S. Dutta, P. Fischer, Nonconforming Schwarz-spectral element methods for incompressible flow, *Computers & Fluids* 191 (2019) 104237. 14

- [38] D. S. Kershaw, Differencing of the diffusion equation in Lagrangian hydrodynamic codes, *Journal of Computational Physics* 39 (2) (1981) 375–395. 15
- [39] T. Kolev, P. Fischer, A. P. Austin, A. T. Barker, N. Beams, J. Brown, J.-S. Camier, N. Chalmers, V. Dobrev, Y. Dudouit, L. Ghaffari, S. Kerkemeier, Y.-H. Lan, E. Merzari, M. Min, W. Pazner, T. Ratnayaka, M. S. Shephard, M. H. Siboni, C. W. Smith, J. L. Thompson, S. Tomov, T. Warburton, CEED ECP milestone report: High-order algorithmic developments and optimizations for large-scale GPU-accelerated simulations, Tech. Rep. WBS 2.2.6.06, CEED-MS36, Exascale Computing Project (2021). 15
- [40] R. Anderson, A. Black, B. Blakeley, R. Bleile, J.-S. Camier, J. Ciurej, A. Cook, V. Dobrev, N. Elliott, J. Grondalski, C. Harrison, R. Hornung, T. Kolev, M. Legendre, W. Liu, W. Nissen, B. Olson, M. Osawe, G. Papadimitriou, O. Pearce, R. Pember, A. Skinner, D. Stevens, T. Stitt, L. Taylor, V. Tomov, R. Rieben, A. Vargas, K. Weiss, D. White, L. Busby, The Multiphysics on Advanced Platforms Project, Tech. rep., LLNL-TR-815869, LLNL (2020). doi:10.2172/1724326. 19
- [41] W. Walters, A brief history of shaped charges, Vol. 1, 24th International Symposium on Ballistics, New Orleans, LA, 2008, pp. 3–10. 19
- [42] V. Dobrev, T. Kolev, R. Rieben, High-order curvilinear finite element methods for Lagrangian hydrodynamics, *SIAM J. Sci. Comp.* 34 (5) (2012) B606–B641. 19

## Appendix A. Source Code for Generating the Kershaw Mesh

In this appendix we provide the C++ code that is used to obtain the initial 3D Kershaw mesh that is optimized in the benchmarks tests of Section 4.1. The initial domain is  $[0, 1]^3$ . Starting with a Cartesian mesh, the deformed configuration is computed by the `kershaw` function that transforms the input coordinates  $x, y, z$  to the deformed positions  $X, Y, Z$ . The deformation is applied to all nodes of the position function  $x$ , see Section 2.1. If the initial Cartesian mesh is  $n_x \times n_y \times n_z$ , then  $n_x$  should be divisible by 6 and  $n_y$  and  $n_z$  should be divisible by 2. The parameters `epsy` and `epsz` correspond to  $\varepsilon_y$  and  $\varepsilon_z$ , see Figure 4.

---

```

1 double right(const double eps, const double x) // 1D transformation at right boundary
2 {
3     return (x <= 0.5) ? (2-eps)*x : 1+eps*(x-1);
4 }
5 double left(const double eps, const double x) // 1D transformation at left boundary
6 {
7     return 1-right(eps,1-x);
8 }
9 double step(const double a, const double b, double x)
10 {
11     if (x <= 0) { return a; }
12     if (x >= 1) { return b; }
13     return a + (b-a)*(x*x*x*(x*(6*x-15)+10)); // Smooth transition from a to b
14 }
15 void kershaw(const double epsy, const double epsz,
16             const double x, const double y, const double z,
17             double &X, double &Y, double &Z) // (x,y,z) -> (X,Y,Z) Kershaw transform
18 {
19     X = x;
20     int layer = x*6.0;
21     double lambda = (x-layer/6.0)*6;
22     switch (layer)
23     {
24     case 0:
25         Y = left(epsy, y);
26         Z = left(epsz, z);
27         break;
28     case 1:
29     case 4:
30         Y = step(left(epsy, y), right(epsy, y), lambda);
31         Z = step(left(epsz, z), right(epsz, z), lambda);
32         break;
33     case 2:
34         Y = step(right(epsy, y), left(epsy, y), lambda/2);
35         Z = step(right(epsz, z), left(epsz, z), lambda/2);
36         break;
37     case 3:
38         Y = step(right(epsy, y), left(epsy, y), (1+lambda)/2);
39         Z = step(right(epsz, z), left(epsz, z), (1+lambda)/2);
40         break;
41     default:
42         Y = right(epsy, y);
43         Z = right(epsz, z);
44         break;
45     }
46 }

```

---